

# 1 Concurrent Bering Sea and Labrador Sea ice melt extremes in March 2 2023: A confluence of meteorological events aligned with 3 stratosphere-troposphere interactions

4 Thomas J. Ballinger<sup>1</sup>, Kent Moore<sup>2,3</sup>, Qinghua Ding<sup>4</sup>, Amy H. Butler<sup>5</sup>, James E. Overland<sup>6</sup>, Richard L.  
5 Thoman<sup>1</sup>, Ian Baxter<sup>4</sup>, Zhe Li<sup>4</sup>, and Edward Hanna<sup>7</sup>

6 <sup>1</sup>International Arctic Research Center, University of Alaska Fairbanks, Fairbanks, AK, USA

7 <sup>2</sup>Department of Physics, University of Toronto, Toronto, Ontario, Canada

8 <sup>3</sup>Department of Chemical and Physical Sciences, University of Toronto, Canada, Toronto, Ontario, Canada

9 <sup>4</sup>Department of Geography, and Earth Research Institute, University of California, Santa Barbara, Santa Barbara, CA, USA

10 <sup>5</sup>Chemical Sciences Laboratory, National Oceanic and Atmospheric Administration, Boulder, CO, USA

11 <sup>6</sup>Pacific Marine Environmental Laboratory, National Oceanic and Atmospheric Administration, Seattle, WA, USA

12 <sup>7</sup>Department of Geography and Lincoln Climate Research Group, University of Lincoln, Lincoln, UK

13

14 *Correspondence to:* Thomas J. Ballinger (tjballinger@alaska.edu)

15 **Abstract.** Today's Arctic is characterized by a lengthening of the sea ice melt season, but also by fast and at times unseasonal  
16 melt events. Such anomalous melt cases have been identified in Pacific and Atlantic Arctic sector sea ice studies. Through  
17 observational analyses, we document an unprecedented, concurrent marginal ice zone melt event in the Bering Sea and  
18 Labrador Sea in March of 2023. Taken independently, variability in the cold season ice edge at synoptic time scales is common.  
19 However, such anomalous, short-term ice loss over either region *during the climatological sea ice maxima* is uncommon, and  
20 the tandem ice loss that occurred qualifies this as a rare event. The atmospheric setting that supported the unseasonal melt  
21 events was preceded by a sudden stratospheric warming event [amidst background La Niña conditions](#) that led to positive  
22 tropospheric height anomalies across much of the Arctic and the development of anomalous mid-troposphere ridges over the  
23 ice loss regions. These large-scale anticyclonic centers funneled extremely warm and moist airstreams onto the ice causing  
24 melt. Further analysis identified the presence of atmospheric rivers within these warm airstreams whose characteristics likely  
25 contributed to this bi-regional ice melt event. Whether such a confluence of anomalous wintertime events associated with  
26 troposphere-stratosphere coupling may occur more often in a warming Arctic remains a research area ripe for further  
27 exploration.

## 28 1 Introduction

29 Observational analyses of the Arctic atmosphere have noted warmer air temperatures and increased moisture content during  
30 the last two decades relative to previous years (Ballinger et al., 2023; Boisvert et al., 2023). Periods of increased climate  
31 variability (Hanna et al., 2015) can coincide with these atmospheric changes in the Arctic to produce extreme meteorological

32 phenomena, which may influence human and environmental systems both within and beyond the high northern latitudes.  
33 Moreover, terrestrial Arctic snow and sea ice extent, area, and depth/thickness control heat exchange between the land, ocean,  
34 and atmosphere (Serreze and Barry, 2011). With less snow and sea ice in a warming Arctic, instances of surface-to-atmosphere  
35 heating perturbations can magnify impacts of synoptic circulation patterns on local and/or remote surface weather extremes  
36 (Francis and Vavrus, 2015; Zhang et al., 2018; Tachibana et al., 2019; Bailey et al., 2021). Thus air-sea interactions resulting  
37 in extreme events in today's Arctic are structurally complex (Walsh et al., 2020) and shaped by the surface condition/type and  
38 prevailing weather pattern (Overland et al., 2021).

39  
40 A key consideration of complex Arctic extreme events is their timing of occurrence within the annual cycle. As an example,  
41 the Arctic Ocean's ice cover tends to thin and decline (thicken and increase) through the boreal summer (winter) months up to  
42 the September minima (March maxima). However, analyses of satellite observations have shown a trend toward earlier melt  
43 onset across most of the Arctic marginal seas (e.g., Stroeve and Notz, 2018) with unusually-timed and often isolated ice loss  
44 events during winter or early spring interspersed on these trends. The North Atlantic Arctic region that includes marginal seas  
45 around Greenland, Iceland, and northwest Europe has experienced several of these cases in recent times. During mid-April of  
46 2013, a persistent anticyclone over Greenland coincided with record-early melt onset in the Baffin Bay, Davis Strait, and  
47 Labrador Sea region that was ~8 weeks earlier than the 1981-2010 average (Ballinger et al., 2018). Above freezing air  
48 temperatures at the North Pole during late December of 2015 led to a substantial loss of sea ice over the Arctic Ocean (Moore,  
49 2016). In late February and early March of 2018, a polynya unexpectedly opened off the northern Greenland coast that was  
50 driven by anomalously warm and strong southerly winds that were preceded by a sudden stratospheric warming (SSW) event  
51 (Moore et al., 2018). In one of the most notable examples, an Arctic cyclone that registered record-low central pressure  
52 traversed the Barents and Kara seas in late January of 2022 and caused record surface winds and attendant ice loss for the time  
53 of year (Blanchard-Wrigglesworth et al., 2022). Unlike the previous cases, dynamical and ocean processes rather than  
54 thermodynamics were attributed to this unseasonal ice loss event.

55  
56 There is a large body of research into so-called compound extreme climate events such as the simultaneous occurrence in a  
57 particular region of a drought and heat wave or a storm surge and fluvial flooding (e.g., Zscheischler et al., 2018; AghaKouchak  
58 et al., 2020). Less well-studied are so-called concurrent climate extreme events where two or more spatially isolated regions  
59 are subject to simultaneous or near-simultaneous extremes (Zhou et al., 2023). Compound events may be associated with a  
60 single overarching phenomenon such as a hurricane, while concurrent events are typically associated with amplified Rossby  
61 Waves (Kornhuber et al., 2020).

62  
63 In this study, we have identified the first known observation of a concurrent climate extreme event in the Arctic as well as one  
64 that is associated with a SSW [and La Niña background state](#). This concurrent event is marked by unusually-timed sea ice melt  
65 in the Bering Sea and Labrador Sea during March of 2023. Our goals in this observationally-based case study are to describe

66 the respective regional sea ice conditions during March 2023, place them in historical spatial and temporal context, and  
67 evaluate the synoptic atmospheric mechanisms responsible for the ensuing melt extremes. As part of our analyses, we evaluate  
68 the probability of such sea ice melt extremes amidst the period that encompassed the climatological Arctic sea ice maximum.  
69 We conclude with a discussion of our findings that considers seasonal and synoptic meteorological anomalies that occurred  
70 during and around the time of these melt events. Our conclusions also touch upon the implications of Arctic warming for  
71 analogous future melt events.

## 72 **2. Data and Methods**

### 73 *2.1 Sea ice and atmospheric datasets*

74 Daily sea ice concentration (SIC in %) is derived from the NOAA/NSIDC Climate Data Record (CDR) of passive microwave  
75 SIC, version 4 (Meier et al., 2021, 2022). This dataset represents a blended product of the NASA Team algorithm (Cavalieri  
76 et al., 1984) and NASA Bootstrap algorithm (Comiso, 1986), and is available daily on a 25 km<sup>2</sup> grid from 1979-onwards.

77  
78 ECMWF fifth generation global atmospheric reanalysis (ERA5) data at their 31 km native resolution for 1979-2023 (Hersbach  
79 et al., 2020) are used to evaluate atmospheric conditions across the Arctic region during and around the SSW event and ensuing  
80 sea-ice melt extremes. ERA5 fields examined include 2-meter air temperature (T2m in °C), total column water vapor (in mm),  
81 total precipitation, which is the sum of large-scale and convective precipitation including rain and snowfall, that reaches the  
82 surface (in mm/day), net and downward longwave radiation (in W/m<sup>2</sup>), and geopotential heights (in m) over the atmospheric  
83 column from 1000 hPa to 1 hPa. Unless otherwise stated, data are binned to daily means. Studies have shown ERA5 to be  
84 effective at capturing Arctic weather and climate variability. As an example, during a research expedition in Fram Strait,  
85 Graham et al. (2019) noted ERA5 air temperatures, humidity, and winds exhibited relatively strong correlations and low biases  
86 in comparison with radiosonde observations and performed better overall than other modern atmospheric reanalyses in the  
87 region. Numerous other studies have relied upon ERA5 data to understand the synoptic evolution and characteristics of  
88 airstreams within the Arctic (e.g., Nygard et al., 2020; Papritz et al., 2022; Kirbus et al., 2023).

89  
90 In addition to reanalysis fields, daily averaged T2m data from regional weather stations are evaluated (**Figure 1**). We  
91 deliberately selected near-coastal weather stations based on several criteria, including multidecadal records that are relatively  
92 complete (>95% of dates surveyed register a T2m value) for sites located north and south of both the early March long-term  
93 mean and 2023 ice edge in the Bering Sea and Labrador Sea, respectively. Data from leap years are omitted as 2023 was not  
94 one. For the Bering Sea region, we obtained T2m data from the National Centers for Environmental Information Applied  
95 Climate Information System (NCEI ACIS) for Alaska terrestrial weather stations at St. Paul (57.16°N, 170.22°W) and  
96 Kotzebue (66.89°N, 162.58°W). The St. Paul historical record is surveyed from 1916-2023, while the Kotzebue record is  
97 assessed from 1923-2023. For the Labrador region two western Greenland weather station records, which are maintained by

98 the Danish Meteorological Institute (DMI), are obtained for Nuuk (64.17°N, 51.75°W) and Aasiaat (68.70°N, 52.75°W). Both  
99 of these Greenland records span 1958 to 2023. We supplement NCEI ACIS and DMI observations with Programme for  
100 Monitoring of the Greenland Ice Sheet (PROMICE) automatic, on-ice weather station temperatures, measured from a nominal  
101 height of 2.7 m above the ice-sheet surface, for two sites: one is near Nuuk on a peripheral glacier (NUK\_K; 64.16°N ,  
102 51.36°W; 710 m asl) and the other is found within the lower ablation area of the Greenland Ice Sheet (GrIS) in the Qassimiut  
103 region (QAS\_L; 61.03°N, 46.85°W; 280 m asl) (Fausto et al., 2021). The PROMICE data records are relatively short, with  
104 NUK\_K established in 2015 and QAS\_L in 2008, though both are 99% complete for the dates we surveyed and provide  
105 valuable information on GrIS in situ air temperatures on the rather observationally sparse Greenland Ice Sheet.

106  
107 Several atmospheric indices are analyzed and discussed in this work. The SSW compendium (Butler et al., 2017, updated), a  
108 long-term archive of indicator climate indices associated with SSW events, confirmed the onset of the late-winter 2023 SSW  
109 event (16 February). We examine one such metric of this archive that we term the Polar Vortex Index (PVI) that describes the  
110 daily-mean, zonal-mean winds at 60°N and 10 hPa, where the timing of the shift from westerly to easterly stratospheric flow  
111 between November and April signifies the SSW onset (Charlton and Polvani, 2007). The PVI is analyzed from 1979-2023.  
112 SSWs are known to influence the mid-to-high latitude tropospheric circulation patterns and often precede a negative North  
113 Atlantic Oscillation (NAO) regime and high-latitude anticyclonic blocking (Baldwin et al., 2021). Therefore, we elect to  
114 analyze the daily NAO and region-specific Greenland Blocking Index (GBI) and Alaska Blocking Index (ABI). The NAO  
115 used here extends from 1950 to 2023 and is defined as the leading, rotated principal component of standardized 500 hPa  
116 geopotential height (z500) anomalies from 20-90°N (Barnston and Livezey, 1987). The GBI describes the mean z500 across  
117 60-80°N, 20-80°W (Hanna et al., 2013), and the ABI depicts the averaged z500 from 55-75°N and 125-180°W (Ballinger et  
118 al., 2022). These blocking indices are analyzed over the 1948 to 2023 period.

119

## 120 2.2 Extreme event detection methods

121 We examine moisture transport into the Arctic during our case study by employing an atmospheric river (AR) detection  
122 algorithm developed by Guan and Waliser (2019). This algorithm is applied on 6-hourly ERA5 integrated water vapor transport  
123 (IVT in kg/m/s) data, averaged from 1000hPa to 300 hPa on a 1.5° x 1.5° global grid. In this framework, ARs for each 6-hour  
124 interval are defined when an IVT threshold exceeding the 85th percentile of climatological IVT is reached for a grid cell in the  
125 domain of interest. Additionally, these ARs must meet specific criteria related to the orientation, length, and length-to-width  
126 ratio of IVT, as outlined by Guan and Waliser (2019). Widely adopted in previous studies spanning the tropics to the high  
127 latitudes including the Arctic and Antarctic, this algorithm serves as a reliable scheme for AR analysis (Collow et al., 2022).  
128 We examine the duration of AR events passing through the Alaska and Greenland regional domains shown in **Figure 1** leading  
129 up to, coinciding with, and following the Bering and Labrador melt events, respectively. AR duration is defined as the  
130 percentage (%) of the day in which an AR resides within any portion of the respective domains. We also measure the intensity  
131 of AR events, defined here as the mean IVT of all grid cells that cross into either domain associated with an AR.

Deleted: 0

133  
134 Daily atmospheric indices and maps of the reanalysis data are presented, and values are identified that meet or exceed an  
135 extreme value threshold (i.e., 95<sup>th</sup> or 99<sup>th</sup> percentile) relative to a specified number of days across the data records described in  
136 Section 2.1. For example, a 99<sup>th</sup> percentile St. Paul, Alaska T2m value during the 90-day “winter” period from 1 January – 31  
137 March 1916-1923 (where 9576 days registered a daily mean T2m reading) is 3.3°C. Use of the full historical period or select  
138 portions of dataset’s records along with extended time windows (e.g., 1 January – 31 March) provided a larger sample size  
139 from which to calculate extreme values relative to the period specified or season (e.g., 90 days) versus a singular date of  
140 reference.

### 141 3. Results

#### 142 3.1 Extreme and unusually-timed sea ice melt

143 The regional SIC means, variability, and anomalies around the peak of the melt events relative to 1-15 March 2000 to 2023  
144 are shown in **Figure 1**. This subset of years is selected as winter months since 2000 have seen a large decline in sea ice  
145 conditions (Stroeve and Notz, 2018). In the Labrador region, the 50% climatological ice edge tilted northeast to southwest  
146 from Davis Strait into the Labrador Sea and transitioned in the marginal ice zone to nearly 100% SIC on the western flank of  
147 this boundary (**Figure 1a**). In contrast, the Bering Sea ice edge exhibited a more zonal orientation and extended from ~61°N  
148 in the western Bering Sea to ~59°N in the eastern Bering Sea (**Figure 1d**). From 2000 to 2023, interannual SIC variability for  
149 the first half of March in these marginal ice zone areas was ~30% (**Figure 1b, e**), while early March 2023 saw SIC reductions  
150 along the ice edge on the order of ~30% (**Figure 1c,f**).

151

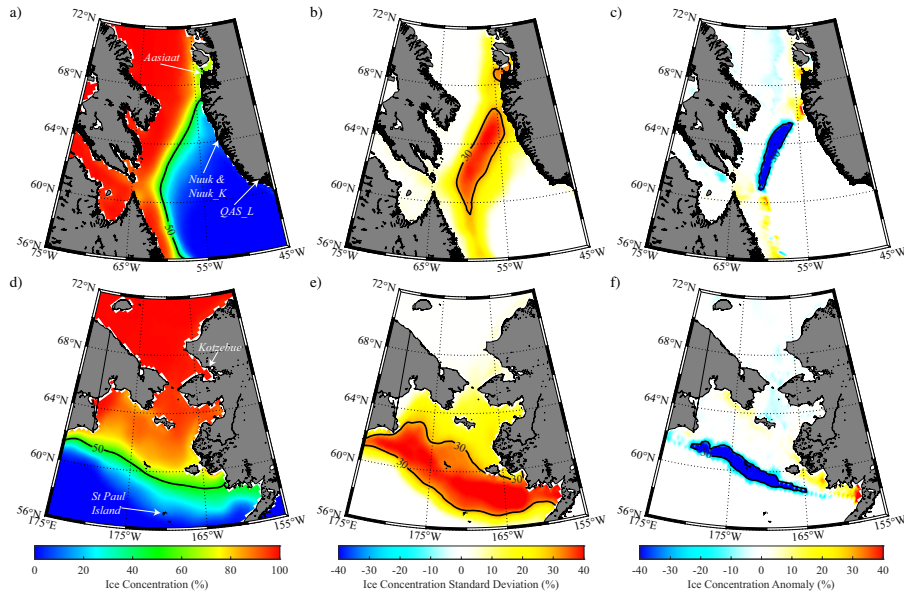


**Figure 1.** Sea ice concentration (SIC in %) from the NOAA/NSIDC CDR dataset. Mean conditions for the period 1-15 March 2000-2023 for: (a) the Labrador Sea and d) the Bering Sea. The SIC standard deviation (%) for 1-15 March 2000-2023 is shown for: (b) the Labrador Sea and e) the Bering Sea. The sea ice concentration anomaly on 5 March 2023 relative to the 1-15 March 2000-2023 period is shown for (c) the Labrador Sea and (f) the Bering Sea. In (a) and (d) locations of the weather stations mentioned in the text are indicated with arrows.

152

153 The SIC conditions in these areas of >30% variability are examined more closely with respect to the winter of 2023. Winter is  
 154 loosely defined here as January through March. From mid-January through February, the daily Labrador SIC exceeded the  
 155 2000-2023 mean, then abruptly plummeted to below-normal conditions in early March and remained below-average through  
 156 the end of the month (**Figure 2a**). The Bering SIC showed more variability about the SIC day-of-year means with periods of  
 157 slightly above and below-normal ice cover into early March and through the rest of the month (**Figure 2b**). While single day  
 158 SIC departures through winter in both areas did not breach the 5<sup>th</sup> or 95<sup>th</sup> percentiles for the day of year, the largest 4-day  
 159 changes (<20% SIC losses) occurred roughly at the same time and culminated on March 5<sup>th</sup> in the Labrador Sea and March 6<sup>th</sup>  
 160 in the Bering Sea (see dashed red vertical lines in **Figure 2**). While day-to-day sea ice variability is not unusual throughout

161 winter, the day-of-year mean curves (thick black lines in **Figure 2**) suggest that ice growth tends to continue in both of these  
162 regions throughout most of March aligned with the typical pan-Arctic sea ice maximum (Meier et al., 2023).  
163

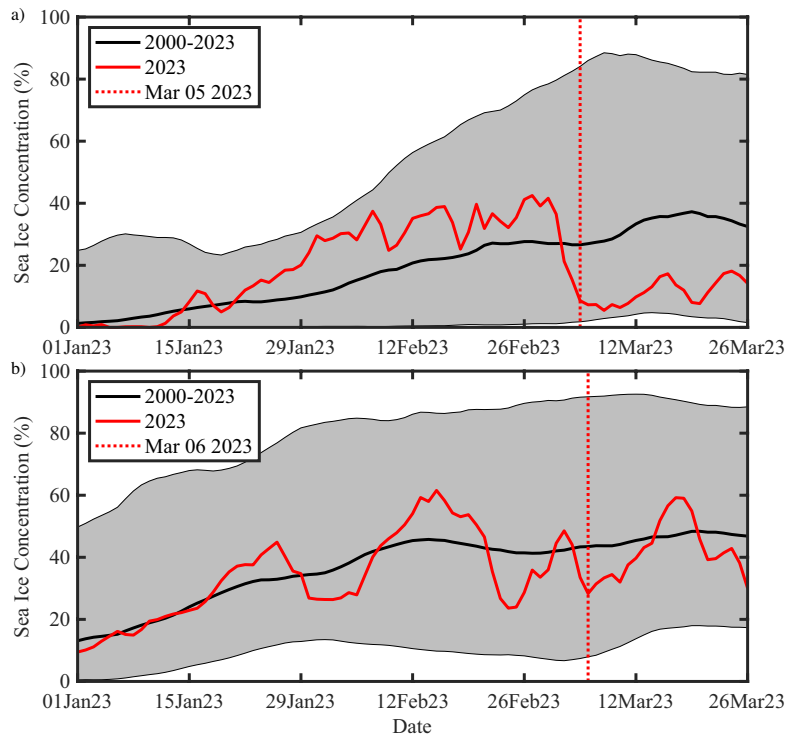


**Figure 2.** Time series (red curves) of the daily SIC averaged over the regions, a) Labrador Sea and b) Bering Sea, respectively in Figures 1b,e, where the standard deviation exceeds 30% for the period 1 January to 26 March 2023. The black line represents the daily mean value for the period 2000-2023 with the shading incorporating daily values between the 5<sup>th</sup> and 95<sup>th</sup> percentile values. The ending dates for the 4-day window with the largest change in ice concentration are shown with the dotted red lines.

164

165 Histograms provide additional probabilistic perspective on the likelihood of such 4-day ice loss events for the times of year  
 166 they occurred in 2023 (**Figure 3**). Since 2000, both the Labrador Sea (red curve) and Bering Sea (blue curve) have shown  
 167 quasi-normal SIC distributions over the 1-15 March period. The 2023 4-day changes in both areas, characterized by ~20% SIC  
 168 reduction in the Bering Sea and ~27% SIC decline in the Labrador Sea, represent extreme outliers found in the far-left tails of  
 169 their respective data distributions. The magnitude of these short-term SIC loss events is uncommon for the time of year, which  
 170 prompts further investigation into the synoptic processes that drive, and potentially link, these rare, concurrent events.

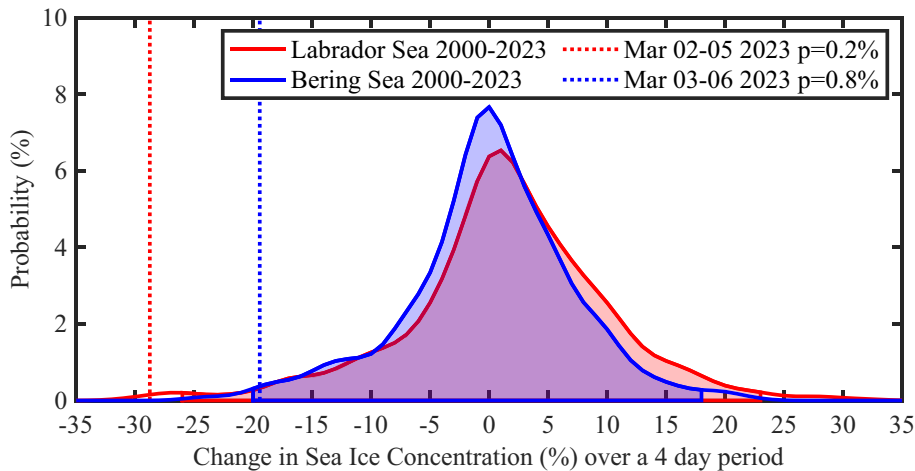


**Figure 3.** Histograms of the change over a 4-day period during 1-15 March 2000-2023 for the Labrador Sea (red) and Bering Sea (blue) regions used in Figure 2. The shading represents the regions bounded by the 1st and 99th percentile values. The largest changes during March 2023 are indicated by the dashed lines.

171 *3.2 Synoptic mechanisms, part 1: The 2023 SSW event and its stratosphere-troposphere signatures*

172 On 16 February, a SSW occurred that appears to have strongly contributed to the synoptic environment in early March that led  
 173 to the cross-Arctic melt events. **Figure 4** shows the winter-long evolution of the height anomalies with respect to the SSW  
 174 event. In mid-January 2023, positive tropospheric heights in the 1000-100 hPa layer preceded positive height anomalies aloft  
 175 that developed toward late January and early February. The positive height anomalies indicate upward troposphere to  
 176 stratosphere coupling that resulted in a minor stratospheric warming event at the end of January. Over the two weeks that  
 177 followed, a second, stronger and positive (~2 sigma) geopotential height anomaly developed aloft within the upper stratosphere

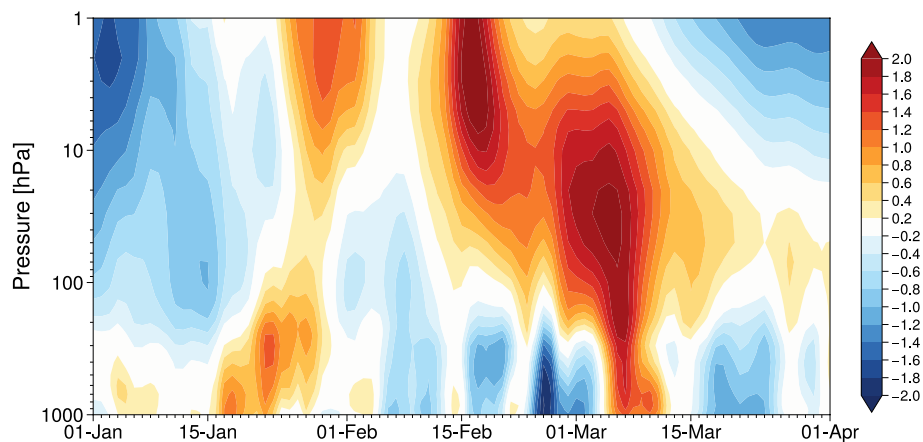
**Deleted:** largely initiated

**Deleted:** conducive



180 and peaked on 16 February in conjunction with the day of the shift from westerly to easterly 10 hPa winds at 60°N found in  
181 the PVI (**Figure 5a**), which marked the date of SSW onset (Butler et al., 2017, updated). The PVI dipped to roughly the 1<sup>st</sup>  
182 percentile following SSW onset on 28 February and 1 March, characterizing this as an anomalously strong event for this time  
183 of year. The PVI reached a minimum wind speed of -18 m/s on 28 February, which places it as the 6<sup>th</sup> strongest reversal (out  
184 of 28 such events) of the polar vortex winds during a stratospheric warming from 1979-2023 (Lee and Butler 2019). As is the  
185 tendency with SSWs, the influence of the above-average, upper stratospheric air pressures and temperatures (latter not shown)  
186 descended during this time, yielding increased heights across the depth of the stratosphere through late February (**Figure 4**).  
187 By early March, the SSW warming signal propagated toward the surface and large positive height anomalies extended through  
188 the depth of the tropospheric column. The largest positive height anomalies within the lower troposphere and at the surface  
189 manifested predominantly over the Greenland/Labrador Sea area (**Figure S1**), as is typical following SSW events (Baldwin et  
190 al., 2021), and the timing coincided with the Bering Sea and Labrador Sea melt events.

191



192

193

194 **Figure 4.** Polar cap (60-90°N) standardized geopotential height anomalies (unitless) from the surface to the upper stratosphere  
195 during winter 2023. The standardized anomalies are calculated at each pressure level by removing the daily climatology and  
196 dividing by the daily standard deviation. The standardized anomalies are shown relative to the day of year for the 1979-2023  
197 period of the ERA5 reanalysis.

198

199 In the two weeks that led up to this strong SSW event, the large-scale mid-tropospheric circulation was characterized by a  
200 positive NAO fluctuation between 0 and 1.5 sigma, indicative of stronger than normal westerly winds across the mid-to-high  
201 latitudes (**Figure 5b**). Negative height anomalies (lower than normal pressure) across most of the polar cap troposphere  
202 between 1-15 February (**Figure 4**) support this assertion. After the SSW event on 16 February, the NAO slightly increased for  
203 two days then plummeted, reversed sign, and became strongly negative ( $\sim -1$  sigma) from 2-8 March around the melt events  
204 (**Figure 5b**). Zooming in on the study regions of interest, strong, lagged ridging responses are noted in the respective mid-  
205 tropospheric height fields. The z500 pattern atop the Labrador Sea area of ice loss described by the GBI is  $>100$  m above-  
206 average from 1-12 March, including record-high day of year departures (since 1948) from 4-7 March when the GBI values  
207 exceeded the 99<sup>th</sup> percentile (**Figure 5c**). This period also corresponded with the strongest downward coupling of the SSW  
208 event to surface conditions (**Figure 4**). While comparatively not as extreme as those of the GBI, ABI values are also  
209 considerably higher-than-average during most of the same period (4-12 March), punctuated by  $>100$  m anomalies from 5-11  
210 March (**Figure 5d**). These higher-than-average ABI values appear related to a persistent high pressure system over the broader  
211 North Pacific region – a signature of the La Niña extratropical teleconnection – that moved into and out of the Alaskan region  
212 on synoptic timescales during the January to March period. As a possible precursor to the SSW event and subsequent pressure  
213 increase through much of the atmospheric column, initially there were ABI peak with values  $>150$  m above-normal from 27-  
214 30 January capped by the 28 January ABI value (5496.83 m) falling just shy of the 99<sup>th</sup> percentile (5501.82 m). The Alaska  
215 ridge (not shown) associated with these elevated ABI values appears well-timed with upward coupling of the troposphere to  
216 the stratosphere (**Figure 4**). We revisit this discussion in **Section 4**.

217

**Deleted:** These late January and mid-March examples could suggest a slow forcing mechanism such as the background La Niña state rendering stronger blocking anticyclones over Alaska.

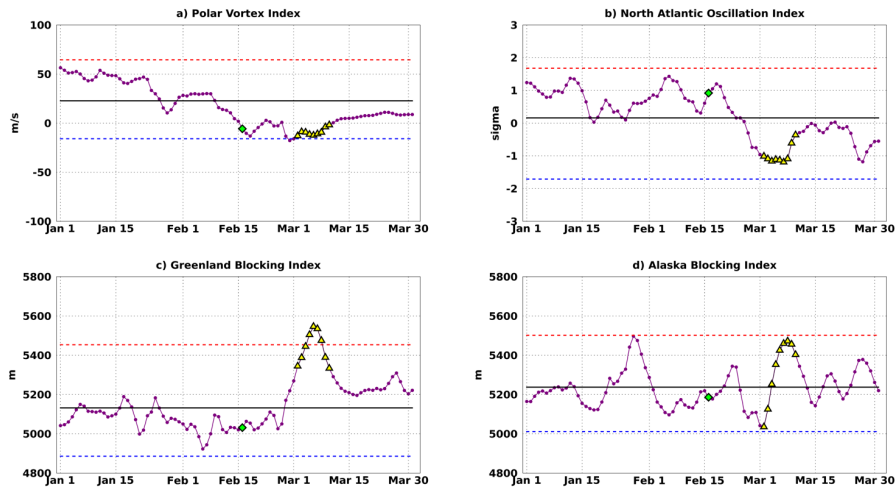
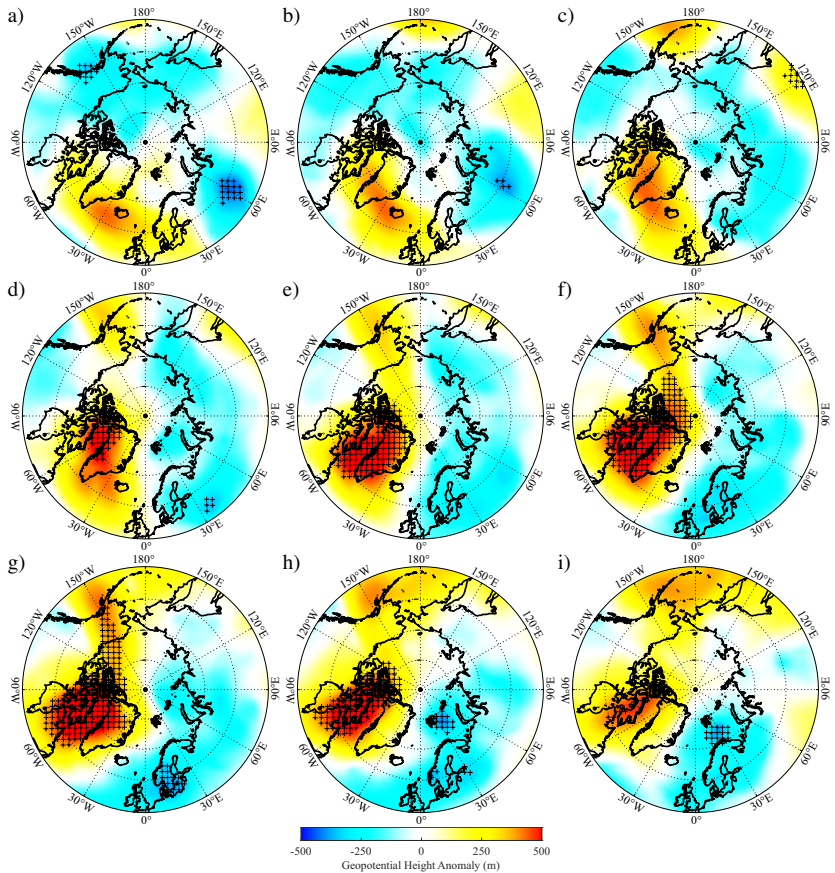


**Figure 5.** Daily atmospheric indices for 1 January – 31 March 2023 (purple lines) overlapping the multi-sectoral melt event for the a) Polar Vortex Index (m/s), b) North Atlantic Oscillation Index (standardized), c) Greenland Blocking Index (m), and d) Alaska Blocking Index (m). Considering all days from 1 January to 31 March for the respective indices' full periods of record (see Section 2.1), the mean of each variable (black line), 1<sup>st</sup> percentile (blue dashed line), and 99<sup>th</sup> percentile (red dashed line) are shown in each graphic. The sudden stratospheric warming event on 16 February 2023 is labeled with a green diamond, and to draw attention to the dates around the Labrador Sea and Bering Sea melt events, the period from 2-10 March 2023 is identified by yellow triangles.

222 The evolution of the day-to-day z500 spatial pattern [in March](#) provides perspective to the values of the large-scale circulation  
223 and regional blocking indices overlapping the melt events. The height pattern over Greenland, Baffin Bay and Labrador Sea  
224 is above-normal and successively strengthens during 2-4 March (**Figure 6a-c**) before the peak in the short-term Labrador Sea  
225 melt observed on 5 March when western Greenland and Baffin Bay is engulfed in >99<sup>th</sup> percentile height anomalies (**Figure**  
226 **6d**). Meanwhile, below-normal mid-tropospheric pressure over Alaska and poleward of the central Bering Sea from 2-4 March  
227 gave way to higher-than average pressure by 5 March and preceded the 6 March peak in the Bering Sea ice loss (**Figure 6e**).  
228 A large-scale dipole structure is evident from 6-10 March, as the North American (Eurasian) high-latitudes spanning the  
229 International Dateline (i.e., 180°W) to ~30°W (30°W-180°W) exhibited higher-than-normal (lower-than-normal) heights with  
230 extreme departures around Greenland (**Figure 6e-i**) that are reflected in the magnitude of the daily GBI anomalies (**Figure**  
231 **5c**). Midtropospheric ridging over high-latitude North America with larger anomalies over Greenland than Alaska represents  
232 a common regional weather regime (Lee et al., 2023), however, the z500 anomalies observed during the latter portion of our  
233 case study are relatively higher in magnitude. In terms of set-up, over the 9-day period, the blocking pattern developed initially  
234 over the Iceland region before retrograding westwards over Greenland towards the Labrador Sea and Baffin Bay. Such  
235 retrograde movements have been noted to occur in other cases of blocking development over the Greenland region (Hanna et  
236 al., 2018). While the z500 pattern orientation and development are not uncommon, the strength of the anticyclonic anomalies  
237 is notable in this case.  
238



239  
 240  
 241 **Figure 6.** 500 hPa geopotential height ( $z_{500}$ ) anomaly (m) from the ERA5 at 0 GMT on: a) 2 March, b) 3 March, c) 4 March,  
 242 d) 5 March, e) 6 March, f) 7 March, g) 8 March, h) 9 March, and i) 10 March 2023. The anomalies are presented with respect  
 243 to the period 16 February – 15 March 1979–2023. Gridpoints where the anomalies are less than the 1st percentile (blue hues)  
 244 or greater than the 99th percentile (red hues) based on the above period are indicated with the '+'.  
 245

246 3.3 Synoptic mechanisms part 2: Thermodynamic effects

247 In the following, we examine the thermodynamic environment overlapping the aforementioned atmospheric circulation  
248 anomalies. **Figure 7** shows the daily pan-Arctic T2m anomaly field (shading) around the melt events; the 0°C isotherm (blue  
249 contour) is overlaid for reference. During 2-4 March, air temperature anomalies over south central Greenland, Davis Strait,  
250 and northern Labrador waters overlapping the ice edge were above-normal (**Figure 7a-c**). In particular, from the 2<sup>nd</sup> to the 3<sup>rd</sup>  
251 of March, the 0°C isotherm abruptly migrated westward and encompassed much of the Labrador Sea including the ice edge  
252 (refer to **Figure 1a**). During this time 99<sup>th</sup> percentile warm extremes were found across the northern Labrador Sea, the southern  
253 tip of Greenland, and the southwestern Irminger Sea. Warm extremes persisted in the vicinity of the ice edge on 5 March  
254 (**Figure 7d**), then the large temperature anomalies (~15-16°C) expanded to cover much of the area from the Labrador Sea  
255 through Baffin Bay on 6-7 March (**Figure 7e,f**). While the warm air mass appeared to propagate westward into northeastern  
256 Canada in the days that followed, T2m anomalies remained above-average in these areas until colder air moved into the region  
257 on 10 March (**Figure 7g-i**).

258  
259 A warm air incursion into the Bering Sea was also apparent during this same time. From the 3<sup>rd</sup> to the 4<sup>th</sup> of March, the 0°C  
260 isotherm migrated several degrees northward as anomalously warm air penetrated into the Bering region (**Figure 7b,c**). The  
261 general southwest to northeast trajectory of the mild airstream was apparent in the days that followed. The 0°C isotherm entered  
262 the northeastern Bering Sea and southwestern Alaska on 5 March as anomalous melt along the ice edge continued, while  
263 temperatures over the western Bering Sea and northeastern Siberia remained below normal (**Figure 7d,e**). Air temperatures  
264 remained above average to extreme in western and northern Alaska during the days that followed as the airmass propagated  
265 into the high Arctic over 6-10 March (**Figure 7f-i**).

**Deleted:** The synoptic set-up following the 2023 SSW event was characterized by mid-tropospheric height increases and development of intense ridging patterns over the Labrador Sea and Bering Sea that spanned the respective regional ice loss events.

**Deleted:** Here

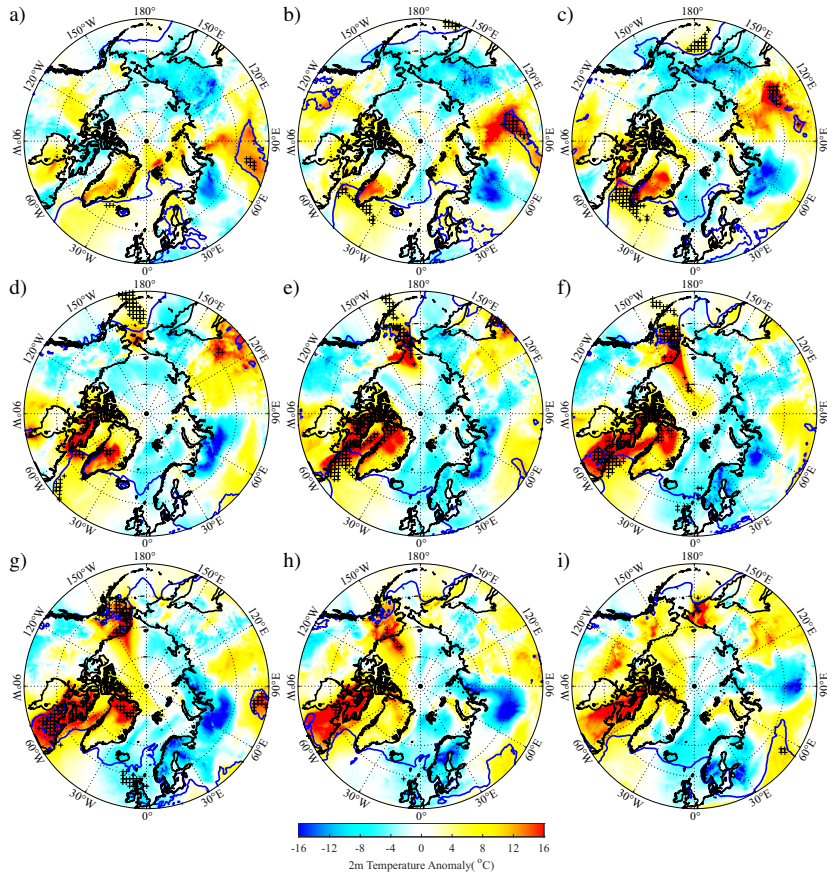


**Figure 7.** Two-meter air temperature anomaly ( $^{\circ}\text{C}$ ) from the ERA5 at 0 GMT on: a) 2 March, b) 3 March, c) 4 March, d) 5 March, e) 6 March, f) 7 March, g) 8 March, h) 9 March, and i) 10 March 2023. The anomalies are shown with respect to the period 16 February – 15 March 1979–2023. Grid points where the anomalies are less than the 1st percentile or greater than the 99th percentile based on the above period are indicated with the '+'. The blue curves represent the  $0^{\circ}\text{C}$  isotherm.

272 Despite the 31 km resolution of the ERA5 fields, the array of synoptic maps makes it challenging to ascertain the extent of the  
273 temperature extremes, especially along coastal areas and along the approximate ice edges. The daily T2m fields are therefore  
274 supplemented with weather station time series to provide additional perspective on the air temperatures. During the Labrador  
275 Sea ice loss event, above-average air temperatures at Nuuk, Greenland to the southeast of the ice edge were recorded with  
276  $>0^{\circ}\text{C}$  daily mean temperatures from 2-7 March with warm air temperature extremes observed on 3-4 March (**Figure 8a**).

277  
278 Likewise, above-freezing, extreme air temperatures were observed in the GrIS lower ablation zone in the Qassimiut region  
279 (QAS\_L) and on a glacier tangential to the Nuuk DMI station (NUK\_K) during this period (**Figure S2a,b**). Meanwhile, in  
280 Aasiaat, Greenland roughly  $\sim 500$  km north of Nuuk, the air temperatures were above-normal during this time, but were not  
281 above-freezing or considered extreme by the criteria used here (**Figure 8b**). Over the Bering Sea, St. Paul Island observed a  
282 stint of above-freezing temperatures that ranked near the 99<sup>th</sup> percentile for 4-7 March (**Figure 8c**), while Kotzebue on Alaska's  
283 northwest coast saw near- to slightly-above normal air temperatures during the Bering ice loss period but the airstream neither  
284 exceeded  $0^{\circ}\text{C}$  nor the 99<sup>th</sup> percentile criteria (**Figure 8d**).

285

Deleted: 1



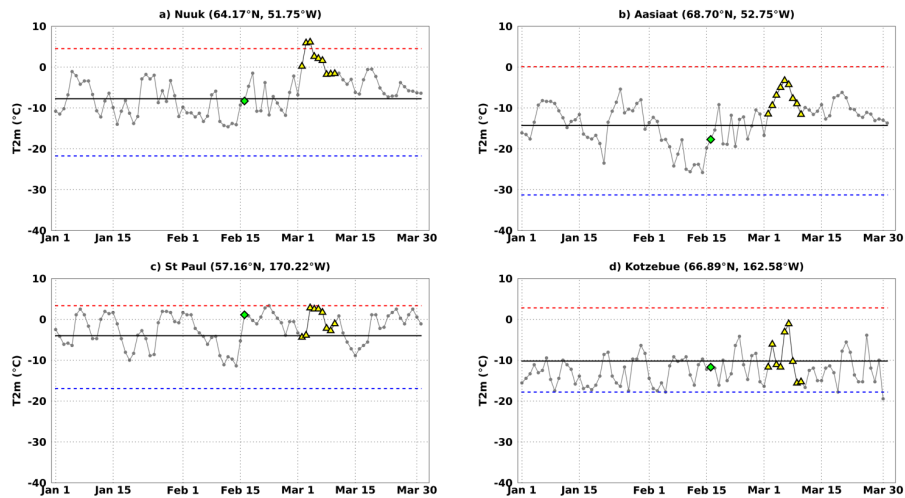


**Figure 8.** Weather station two-meter air temperature ( $^{\circ}\text{C}$ ) 1 January – 31 March 2023 daily time series (gray lines) overlapping the multi-sectoral melt event for a) Nuuk, b) Aasiaat, c) St. Paul, and d) Kotzebue. Considering all days from 1 January to 31 March for the respective stations' full periods of record (see Section 2.1), the mean T2m (black line), 1<sup>st</sup> percentile (blue dashed line), and 99<sup>th</sup> percentile (red dashed line) are shown in each graphic. The sudden stratospheric warming event on 16 February 2023 is labelled with a green diamond, and to draw attention to the dates around the Labrador Sea and Bering Sea melt events, the period from 2-10 March 2023 is identified by yellow triangles. For reference the weather stations are overlaid on **Figure 1**.

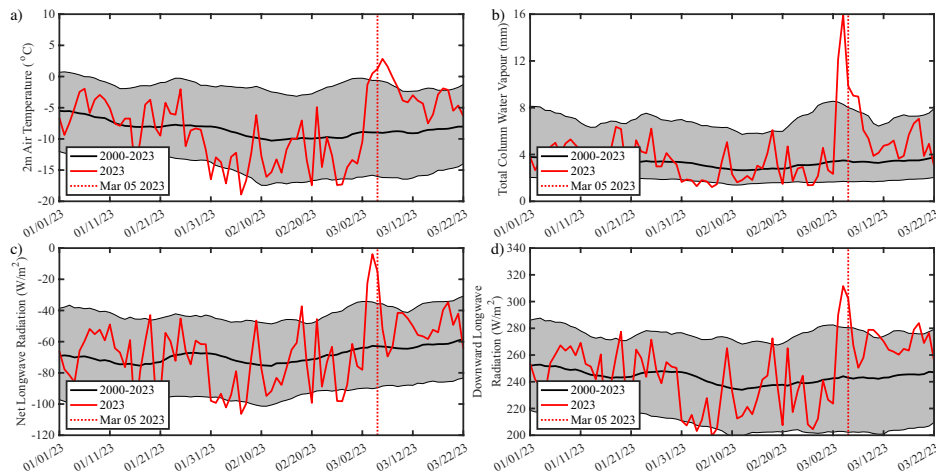
Deleted: T2m in

288 Further analysis into the thermodynamic environment revealed that the anomalously warm airstreams advected over both the  
 289 Labrador and Bering regions possessed extreme water vapor content around the time of their respective melt peaks shown in  
 290 time series in **Figure 9a,b** and **Figure 10a,b** and in maps presented in **Figure S3**. During these peaks, both seas experienced  
 291 anomalous net and downwelling radiation in excess of the 95<sup>th</sup> percentile (**Figures 9c,d** and **Figures 10c,d**) with that energy  
 292 likely driving ice loss through melt. To further investigate the hydrometeorological nature of these airstreams the Guan and  
 293 Waliser (2019) atmospheric river (AR) detection algorithm was run separately for the Labrador Sea and Bering Sea domains  
 294 shown in **Figure 1**. Warm, moist conditions that overlapped these melt events were associated with AR activity (**Figure 11**).  
 295 An AR resided over the Labrador Sea for >40% of the day on 3-4 March, and its residence time was extreme on 5 March

Deleted: 2

297 (~60% of the day; **Figure 11a**). Moisture within this AR (**Figure 11c**) and total precipitation from the AR (**Figure S4**) were  
 298 both above-average, but not extreme. Meanwhile, daily AR residence time within the Bering Sea exceeded 40% on 4-7 March,  
 299 with an AR duration extreme (>60% of the day) on 5 March preceding the short-term melt peak on 6 March when IVT was  
 300 also extreme (**Figure 11b,d**). Extreme ERA5 daily precipitation associated with the AR intrusion fell in the Bering region  
 301 from 5-8 March (**Figure S4**). These persistent and anomalously warm and wet airmasses contributed to these tandem melt  
 302 extremes. Further analysis is ongoing to examine the full surface energy budget, including the role of rainfall, toward shaping  
 303 the observed melt.

304



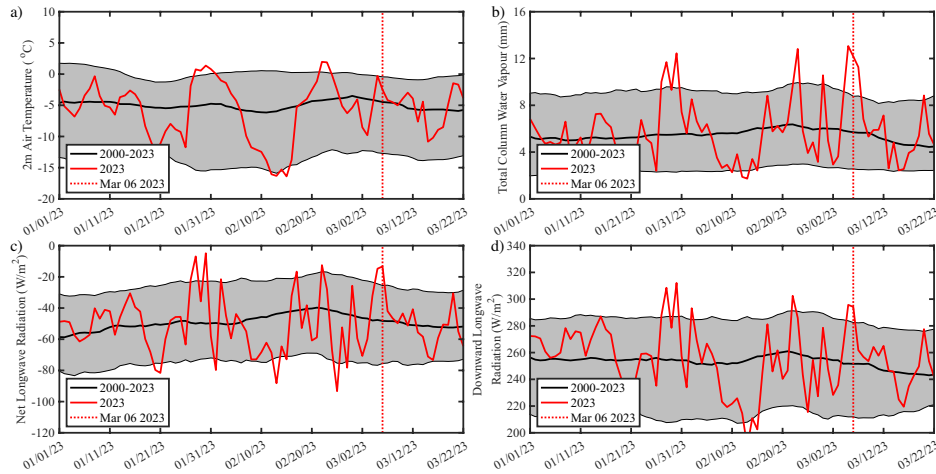
305

306

307 **Figure 9.** Time series (red curves) of ERA5: a) two-meter air temperature ( $^{\circ}\text{C}$ ), b) total column water vapor (mm), c) net  
 308 longwave radiation ( $\text{W}/\text{m}^2$ ), and d) downward longwave radiation ( $\text{W}/\text{m}^2$ ) averaged over the Labrador Sea region, indicated  
 309 in Figure 1b, for the period January 1 to March 26, 2023. The black line represents the climatological mean value for the period  
 310 2000-2023 with shading incorporating values between the 5<sup>th</sup> and 95<sup>th</sup> percentiles. The ending date for the 4-day window with  
 311 the largest change in sea ice concentration is shown with the dotted red line.

312

313



314  
 315  
 316 **Figure 10.** Time series (red curves) of ERA5: a) two-meter air temperature ( $^{\circ}\text{C}$ ), b) total column water vapor (mm), c) net  
 317 longwave radiation ( $\text{W}/\text{m}^2$ ), and d) downward longwave radiation ( $\text{W}/\text{m}^2$ ) averaged over the Bering Sea region, indicated in  
 318 Figure 1e, for the period January 1 to March 26, 2023. The black line represents the climatological mean value for the period  
 319 2000-2023 with shading incorporating values between the 5<sup>th</sup> and 95<sup>th</sup> percentiles. The ending date for the 4-day window with  
 320 the largest change in sea ice concentration is shown with the dotted red line.

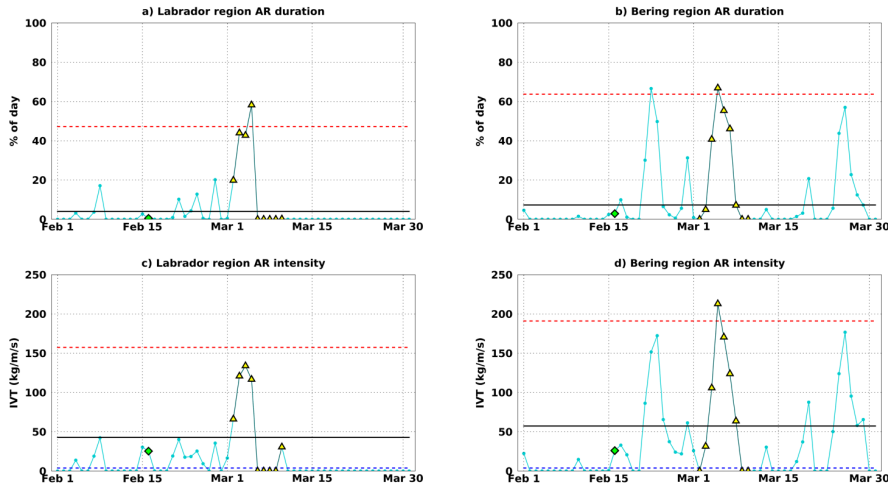


**Figure 11.** March atmospheric river (AR) duration (% of day AR in domain) and intensity (kg/m/s) for the Labrador region (a,c) and Bering region (b,d), respectively (teal lines). The AR data are calculated over the same domains as shown in **Figure 1**. The thick black line in each panel represents the 1979-2023 mean. Considering all days from 1 February to 31 March for the respective regions for the 1979 to 2023 period, the 99<sup>th</sup> percentile (red dashed lines) are shown in all panels while the 1<sup>st</sup> percentile represents AR non-occurrence, and therefore is not marked in these plots. The sudden stratospheric warming event on 16 February 2023 is labelled with a green diamond, and to draw attention to the dates around the Labrador Sea and Bering Sea melt events, the period from 2-10 March 2023 is identified by yellow triangles.

#### 4. Discussion and conclusions

321 Tandem, unusually-timed sea ice melt extremes in the Bering Sea and Labrador Sea occurred in early March 2023. The retreat  
 322 of the ice edge in both marginal seas was similarly driven by the confluence of anomalous meteorological phenomena, Mid-  
 323 tropospheric heights increased and intense ridging patterns developed over the Labrador Sea and Bering Sea during the time  
 324 in which the respective regional ice loss events occurred. A longitude-pressure analysis (Figure S1) revealed that a SSW in  
 325 February 2023 was strongly linked to the mid-tropospheric height increases over the Labrador Sea region in early March, while  
 326 the height increases over the Bering Sea were isolated to the troposphere, and were likely linked to a fortuitous shift of the  
 327 large-scale La Nina-related ridging over the North Pacific into the Alaskan region. Below we discuss the ice loss events and  
 328 focus on the attendant atmospheric mechanisms that provided thermodynamic support for their occurrence.

**Deleted:** following an SSW event that occurred in mid-February

330  
331 *4.1 Perspectives on ice losses during the maximum and supporting atmospheric processes*  
332 Amidst the decline of winter season ice coverage and thickness in the warming Arctic, the latitude of the ice edge can vary on  
333 daily timescales due to wind and melt-driven processes. However, the probability curves shown in **Figure 3** suggest that such  
334 short-term March 2023 sea ice losses in either the Bering or Labrador regions, taken independently, qualify as extreme events.  
335 Both the magnitude of losses and the unusual timing of their anomalous occurrence aligned with the climatological Arctic sea  
336 ice maximum may further qualify these melt extremes collectively as a rare synoptic ice loss event. We do not assess ice edge  
337 changes in other marginal seas during the March historical record to establish whether other areas participated in this event.  
338  
339 The anatomy of the melt extremes can be described by a confluence of anomalous atmospheric phenomena that simultaneously  
340 occurred over the Bering Sea and Labrador Sea. The melt period was preceded by an SSW event that led to a shift in the large-  
341 scale mid-tropospheric circulation regime over the polar cap as evidenced by the rapid transition over two weeks from strong  
342 positive to negative NAO conditions and lower to higher mid-tropospheric air pressure over the high Arctic, in particular over  
343 Greenland. The noted shift to negative NAO followed by the development of a Greenland block that supported southerly winds  
344 and warm advection across the Labrador Sea following a SSW has been documented in previous studies (e.g., Charlton-Perez  
345 et al., 2018; Domeisen, 2019; Domeisen and Butler, 2020). While the set-up of the Greenland block is not unique to this event,  
346 its magnitude for the time of year is remarkable as shown by the extremes highlighted in the GBI time series (**Figure 5c**) and  
347 z500 spatial plots (**Figure 6**).  
348  
349 SSWs on average tend to elicit a weaker atmospheric dynamical response over the Bering region than the Labrador Sea. Smith  
350 et al. (2018) analyzed data from the Whole Atmosphere Community Climate Model of NCAR's Community Earth System  
351 Model and found that over the 40 days following SSW onset there were minimal sea-level pressure (SLP) changes over the  
352 Bering Sea and greater Alaska, but there were large, positive SLP anomalies located northward and eastward of these areas  
353 including around Greenland. Across SSW winters (JFM), the authors also found similar SLP signatures over Greenland, but  
354 negative SLP anomalies and northerly winds over Alaska and the Bering Sea. However, if we consider only SSWs that occur  
355 during La Niña winters, the large-scale circulation response following these events (Figure S5b) looks very similar to the  
356 patterns seen in 2023 (Figure S5a), with ridging over both Greenland and the Aleutians. The interpretation is that the SSW  
357 drives most of the tropospheric height changes over Greenland and the North Atlantic, while, La Niña background conditions  
358 favor North Pacific ridging into the Gulf of Alaska. In addition to the SSW event and La Niña phase, factors such as internal  
359 variability of the climate system and air-sea interactions over the North Pacific Ocean may have played a role in inducing the  
360 anomalously strong mid-tropospheric ridge extending from Greenland to Alaska.  
361  
362 In both the Labrador Sea and Bering Sea, anomalous atmospheric circulation characteristics, namely the stationary, extreme  
363 blocking anticyclones, supported southerly advection of above-normal to extremely warm and moist air that led to these

**Deleted:** of the large-scale circulation pattern is complicated by the La Niña phase that prevailed during winter 2023 (**Figure S3a**).

**Deleted:** s

**Deleted:** with low pressure across the Bering Strait and Pacific Arctic (**Figure S3b**)

**Deleted:** However, compared to the average conditions that occur after SSWs during La Niña winters, March 2023 was marked by a relatively stronger North Pacific ridge that extended further north over Bering Sea and mainland Alaska. These anomalously high mid-tropospheric heights, reflected by an increase in the ABI (**Figure 5d**) and shown in the positive z500 anomaly maps from 5-10 March (**Figure 6d-i**), drove warm advection that caused Bering Sea ice to melt. ...

377 thermodynamically-driven melt events (e.g., **Figures 7, 9-11, and Figure S2**). Additional investigation of the airstreams  
378 revealed that anomalous ARs were present in both regions during this time and played a critical role in the simultaneous melt  
379 extremes. The extreme duration of the AR over the peak Labrador Sea melt and extreme duration and intensity immediately  
380 preceding the Bering Sea melt, both on 5 March, likely enhanced downwelling longwave energy transfer into the ice, causing  
381 its short-term, yet remarkable, decline. Past studies have likewise identified downward longwave radiative flux during AR  
382 passage as a key process that tends to decrease ice mass balance during summer (Mattingly et al., 2018; Wille et al., 2019;  
383 Francis et al., 2020) and slows wintertime ice growth (Hegyi and Taylor, 2018; Zhang et al., 2023). Here, we document the  
384 role of anomalous large-scale meteorological characteristics, including tandem AR events, that drove unprecedented and  
385 concurrent sea ice melt at a time of year characterized by maximum ice extent.

386

#### 387 *4.2 Additional considerations emanating from this case study*

388 This rare ice loss event concurrently encompassing the Bering Sea and Labrador Sea was shaped by a confluence of synoptic  
389 extremes that aligned in time to induce thermodynamic melt of the sea ice edge. We look at this ice loss from a thermodynamic  
390 perspective, though concede that in addition to supporting melt that southerly winds could have induced some sea ice  
391 compaction in the marginal ice zones through convergence. If this event was examined through a sea ice budget lens, we  
392 acknowledge that producing estimates of ice dynamical processes, such as wind-driven convergence and divergence, would  
393 be important to gain a more complete understanding of the evolution of mechanisms responsible for these regional ice losses.  
394 Follow-on work will take a broader view of thermodynamic processes, which may provide additional insight into ice loss  
395 mechanisms elucidated in this case study. For example, resolution of the sea ice types and surface energy balance before,  
396 during, and after the melt event may provide perspectives on ice-air interactions that shaped it.

397

398 Related to the surface energy balance processes, further analyses will delve deeper into the roles of latent heating and humidity  
399 fluxes in shaping the ice melt event. Rainfall (<1 mm) was observed during 2-3 March in the rain gauges at the Nuuk and  
400 Aasiaat DMI weather stations, and, if it were not for sporadic station outages from 2-10 March, rain on other days during this  
401 period may have been documented (C. Drost Jensen 2024, personal communication). Nearby, separate near-coastal weather  
402 stations maintained by Asiaq Greenland Survey also documented small amounts (<1 mm) of rainfall at Nuuk and Kobbefjord  
403 (A. Ginnerup 2024, personal communication). Meanwhile, terrestrial weather stations at Kotzebue and Nome, Alaska, ~300  
404 km to the southwest, saw >25 mm of cumulative rainfall during 4-6 March, which are 3-day total precipitation records for both  
405 weather stations in March (R. Thoman 2023, personal communication). Spatial patterns of ERA5 total precipitation over this  
406 period are consistent with these observations (**Figure S4**). In addition to rain measurements near the coast, rain on cold snow  
407 was also detected in weather station observations found in the southwestern GrIS accumulation zone, which is rare for the time  
408 of year (J. Box 2024, personal communication). Further diagnostic evaluation is needed to determine the extent, frequency,  
409 amount, and impacts of rainfall on the cold snow cover on the GrIS and sea ice during this period. Thus, follow-on studies of

410 the surface energy exchange processes and precipitation characteristics may help to broaden our perspective of this complex  
411 extreme event.

412  
413 It is clear from recent years that there are occurrences of a variety of extreme Arctic events that vary in location, season, and  
414 type which meet or exceed previous records (Walsh et al. 2020). Philosophically, it is difficult to project let alone interpret the  
415 future frequency of these events without detailed historical analogues. It has been proposed that the recent increase of Arctic  
416 extremes is due to an overlap of steadily increasing Arctic warming that is constructively superimposed on the natural range  
417 of atmospheric and oceanic dynamics, e.g., jet stream meanders, atmospheric blocking, storms, and upper-ocean heat content  
418 (Overland 2022), which could themselves, at least in some cases, be influenced by anthropogenic global heating. This is  
419 certainly the case with the concurrent examples from the Labrador Sea and Bering Sea in March 2023. Whether this extreme  
420 event foreshadows a more frequent occurrence of similar events in the future is an open but intriguing question that merits  
421 careful future investigation.

422  
423 *Data availability.* Alaska weather station data are available from <https://xmacis.rcc-acis.org>. Greenland coastal weather station  
424 records were obtained from Caroline Drost Jensen (DMI). PROMICE observations are from  
425 <https://dataverse.geus.dk/dataset.xhtml?persistentId=doi:10.22008/FK2/IW73UU>. The NAO index was downloaded from  
426 <https://www.cpc.ncep.noaa.gov/products/precip/CWlink/pna/nao.shtml>. ERA5 reanalysis fields are obtained from the  
427 Copernicus Climate Data Store at [https://cds.climate.copernicus.eu/cdsapp#!/dataset/reanalysis-era5-single-](https://cds.climate.copernicus.eu/cdsapp#!/dataset/reanalysis-era5-single-levels?tab=overview)  
428 [levels?tab=overview](https://cds.climate.copernicus.eu/cdsapp#!/dataset/reanalysis-era5-single-levels?tab=overview). Sea ice data are downloaded from NSIDC at <https://nsidc.org/data/g02202/versions/4>. The SSW  
429 Compendium can be found at <https://csl.noaa.gov/groups/csl8/sswcompendium/majorevents.html>.

430  
431 *Author contributions.* T.B. and G.W.K.M. conceived the study with input from Q.D., A.H.B., J.E.O., R.L.T., I.B., Z.L., and  
432 E.H. as the study developed. R.L.T. provided assistance with data acquisition. All authors provided feedback on draft iterations  
433 of the paper.

434  
435 *Competing Interests.* None.

436  
437 *Acknowledgements.* T.J.B. and Q.D. were funded by NSF Arctic System Science awards 2246600 and 2246601, respectively.  
438 J.E.O. is supported by NOAA's GOMO Arctic Research Program. PMEL contribution #53XX. GWKM was funded by the  
439 Natural Sciences and Engineering Research Council of Canada. E.H. was supported by NERC NE/W005875/1. The authors  
440 wish to thank Caroline Drost Jensen and Anders Ginnerup for assistance obtaining and interpreting the Greenland weather  
441 station records. We also thank numerous scientists for discussions on topics related to high-latitude precipitation and GrIS  
442 meteorology, including Jason Box, Jakob Abermann, Matthew Sturm, and Melinda Webster.

443 **References**

- 444 AghaKouchak, A., Chiang, F., Huning, L.S., Love, C.A., Mallakpour, I., Mazdiyasni, O., Moftakhari, H., Papalexiou, S.M.,  
445 Ragno, E., and Sadegh, M.: Climate Extremes and Compound Hazards in a Warming World. *Ann. Rev. Earth Planet. Sci.*, 48,  
446 <https://doi.org/10.1146/annurev-earth-071719-055228>, 2020.
- 447
- 448 Baldwin, M.P., Ayarzagüena, B. Birner, T., Butchart, N., Butler, A.H., Charlton-Perez, A.J., Domeisen, D.I.V., Garfinkel,  
449 C.I., Garny, H., Gerber, E.P., Hegglin, M.I., Langematz, U., and Pedatella, N.M.: Sudden Stratospheric Warmings. *Rev.*  
450 *Geophys.*, 59, e2020RG000708, <https://doi.org/10.1029/2020RG000708>, 2021.
- 451
- 452 Bailey, H., Hubbard, A., Klein, E.S., Mustonen, K.-R., Akers, P.D., Marttila, H., and Welker, J.M.: Arctic sea-ice loss fuels  
453 extreme European snowfall. *Nat. Geosci.*, 14, 283-288, <https://doi.org/10.1038/s41561-021-00719-y>, 2021.
- 454
- 455 Ballinger, T.J., Hanna, E., Hall, R.J., Cropper, T.E., Miller, J., Ribergaard, M.H., Overland, J.E., and Høyer, J.L.: Anomalous  
456 blocking over Greenland preceded the 2013 extreme early melt of local sea ice. *Ann. Glaciol.*, 59, 181-190,  
457 <https://doi:10.1017/aog.2017.30>, 2018.
- 458
- 459 Ballinger, T.J., Walsh, J.E., Alexeev, V.A., Bieniek, P.A., McLeod, J.T.: The Alaska Blocking Index, version 2: Analysis and  
460 covariability with statewide and large-scale climate from 1948-2020. *Int. J. Climatol.*, 42, 9767-9787,  
461 <https://doi:10.1002/joc.7864>, 2022.
- 462
- 463 Ballinger, T.J., Overland, J.E., Wang, M., Bhatt, U.S., Brettschneider, B., Hanna, E., Hanssen-Bauer, I., Kim, S.-J., Thoman,  
464 R.L., and Walsh, J.E.: Surface air temperature [in “State of the Climate in 2022”]. *Bull. Am. Meteor. Soc.*, 104, S279-S281,  
465 <https://doi:10.1175/10.1175/BAMS-D-23-0079.1>, 2023.
- 466
- 467 Barnston, A.G., and Livezey, R.E.: Classification, seasonality, and persistence of low-frequency atmospheric circulation  
468 patterns. *Mon. Wea. Rev.*, 115, 1083-1126, [https://doi.org/10.1175/1520-0493\(1987\)115<1083:CSAPOL>2.0.CO;2](https://doi.org/10.1175/1520-0493(1987)115<1083:CSAPOL>2.0.CO;2), 1987.
- 469
- 470 Blanchard-Wrigglesworth, E., Webster, M., Boisvert, L., Parker, C., and Horvat, C.: Record Arctic cyclone of January 2022:  
471 Characteristics, impacts, and predictability. *J. Geophys. Res. – Atmos.*, 127, e2022JD037161,  
472 <https://doi.org/10.1029/2022JD037161>, 2022.
- 473
- 474 Boisvert, L., Parker, C., and Valkonen, E.: A warmer and wetter Arctic: Insights from a 20-years AIRS record. *J. Geophys.*  
475 *Res. – Atmos.*, 128, e2023JD038793, <https://doi.org/10.1029/2023JD038793>, 2023.

Deleted: 0



477  
478 Butler, A.H., Sjoberg, J.P., Seidel, D.J., and Rosenlof, K.H.: A sudden stratospheric warming compendium. *Earth Syst. Sci.*  
479 *Data*, 9, 63-76, <https://doi.org/10.5194/essd-9-63-2017>, 2017.  
480  
481 Cavaliere, D., Gloersen, P., and Campbell, W.J.: Determination of sea ice parameters with the NIMBUS-7 SMMR. *J. Geophys.*  
482 *Res.*, 89 (D4), 5355-5369, <https://doi.org/10.1029/JD089iD04p05355>, 1984.  
483  
484 Charlton, A.J., and Polvani, L.M.: A new look at Stratospheric Sudden Warmings: Part I: Climatology and modeling  
485 benchmarks. *J. Climate*, 20, 449-469, <https://doi.org/10.1175/JCLI3996.1>, 2007.  
486  
487 Charlton-Perez, A.J., Ferranti, L., and Lee, R.W.: The influence of the stratospheric state on North Atlantic weather regimes.  
488 *Q.J.R. Meteorol. Soc.*, 144, 1140-1151, <https://doi.org/10.1002/qj.3280>, 2018.  
489  
490 Collow, A.B.M., Shields, C.A., Guan, B., Kim, S., Lora, J.M., McClenny, E.E., Nardi, K., Payne, A., Reid, K., Shearer, E.J.,  
491 Tomé, R., Wille, J.D., Ramos, A.M., Gorodetskaya, I.V., Leung, L.R., O'Brien, T.A., Ralph, F.M., Rutz, J., Ullrich, P.A.,  
492 Wehner, M.: An overview of ARTMIP's Tier 2 Reanalysis Intercomparison: Uncertainty in the detection of atmospheric rivers  
493 and their associated precipitation. *J. Geophys. Res. – Atmos.*, 127, e2021JD036155, <https://doi.org/10.1029/2021JD036155>,  
494 2022.  
495  
496 Comiso, J.C.: Characteristics of Arctic winter sea ice from satellite multispectral microwave observations. *J. Geophys. Res. –*  
497 *Oceans*, 91 (C1), 975-994, <https://doi.org/10.1029/JC091iC01p00975>, 1986.  
498  
499 Domeisen, D.I.V.: Estimating the frequency of sudden stratospheric warming events from surface observations of the North  
500 Atlantic Oscillation. *J. Geophys. Res. Atmos.*, 124, 3180-3194, <https://doi.org/10.1029/2018JD030077>, 2019.  
501  
502 Domeisen, D.I.V., and Butler, A.H.: Stratosphere drivers of extreme events at the Earth's surface. *Comm. Earth Environ.*, 1,  
503 59, <https://doi.org/10.1038/s43247-020-00060-z>, 2020.  
504  
505 Fausto, R. S., van As, D., Mankoff, K. D., Vandecrux, B., Citterio, M., Ahlström, A. P., Andersen, S. B., Colgan, W., Karlsson,  
506 N. B., Kjeldsen, K. K., Korsgaard, N. J., Larsen, S. H., Nielsen, S., Pedersen, A. Ø., Shields, C. L., Solgaard, A. M., and Box,  
507 J. E.: Programme for Monitoring of the Greenland Ice Sheet (PROMICE) automatic weather station data, *Earth Syst. Sci. Data*,  
508 13, 3819–3845, <https://doi.org/10.5194/essd-13-3819-2021>, 2021.  
509

510 Francis, J.A., and Vavrus, S.J.: Evidence for a wavier jet stream in response to rapid Arctic warming. *Environ. Res. Lett.*, 10,  
511 014005, <https://doi.org/10.1088/1748-9326/10/1/014005>, 2015.

512

513 Francis, D., Mattingly, K.S., Temmi, M., Massom, R., and Heil, P.: On the crucial role of atmospheric rivers in the two major  
514 Weddell Polynya events in 1973 and 2017 in Antarctica. *Sci. Adv.*, 6, <https://doi.org/10.1126/sciadv.abc2695>, 2020.

515

516 Graham, R.M., Hudson, S.R., and Matarilli, M.: Improved performance of ERA5 in Arctic gateway relative to four global  
517 atmospheric reanalyses. *Geophys. Res. Lett.*, 46, 6138-6147, <https://doi.org/10.1029/2019GL082781>, 2019.

518

519 Guan, B., and Waliser, D.E.: Tracking atmospheric rivers globally: spatial distributions and temporal evolution of life cycle  
520 characteristics. *J. Geophys. Res.*, 124, 12523–12552, <https://doi.org/10.1029/2019JD031205>, 2019.

521

522 Hanna, E., Jones, J.M., Cappelen, J., Mernild, S.H., Wood, L., Steffen, K., and Huybrechts, P.: The influence of North Atlantic  
523 atmospheric and oceanic forcing effects on 1900-2010 Greenland summer climate and ice melt/runoff. *Int. J. Climatol.*, 33,  
524 862-880, <https://doi.org/10.1002/joc.3475>, 2013.

525

526 Hanna, E., Cropper, T.E., Jones, P.D., Scaife, A.A., and Allan, R.: Recent seasonal asymmetric changes in the NAO (a marked  
527 summer decline and increased winter variability) and associated changes in the AO and Greenland Blocking Index. *Int. J.*  
528 *Climatol.*, 35, 2540-2554, <https://doi.org/10.1002/joc.4157>, 2015.

529

530 Hanna, E., Hall, R.J., Cropper, T.E., Ballinger, T.J., Wake, L., Mote, T., and Cappelen, J.: Greenland blocking index daily  
531 series 1851-2015: Analysis of changes in extremes and links with North Atlantic and UK climate variability and change. *Int.*  
532 *J. Climatol.*, 38, 3546-3564, <https://doi.org/10.1002/joc.5516>, 2018.

533

534 Hegyi, B.M., and Taylor, P.C.: The unprecedented 2016-2017 Arctic sea ice growth season: The critical role of atmospheric  
535 rivers and longwave fluxes. *Geophys. Res. Lett.*, 45, 5204-5212, <https://doi.org/10.1029/2017GL076717>, 2018.

536

537 Hersbach, H., Bell, B., Berrisford, P., Hirahara, S., Horányi, A., Muñoz-Sabater, J., Nicolas, J., Peubey, C., Radum, R.,  
538 Schepers, D., Simmons, A., Soci, C., Abdalla, S., Abellan, X., Balsamo, G., Bechtold, P., Biavati, G., Bidlot, J., Bonavita, M.,  
539 De Chiara, G., Dahlgren, P., Dee, D., Diamantakis, M., Dragani, R., Flemming, J., Forbes, R., Fuentes, M., Geer, A.,  
540 Haimberger, L., Healy, S., Hogan, R.J., Hólm, E., Janisková, M., Keeley, S., Laloyaux, P., Lopez, P., Lupu, C., Radnoti, G.,  
541 de Rosnay, P., Rozum, I., Vamborg, F., Villaume, S., and Thépaut, J.-N.: The ERA5 Global Reanalysis. *Q.J. R. Meteorol.*  
542 *Soc.*, 146, 1999-2049, <https://doi.org/10.1002/qj.3803>, 2020.

543

544 Kirbus, B., Tiedeck, S., Camplani, A., Chylik, J., Crewell, S., Dahlke, S., Ebell, K., Gorodetskaya, I., Griesche, H., Handorf,  
545 D., Höschel, I., Lauer, M., Neggers, R., Rückert, J., Shupe, M.D., Spreen, G., Walbröl, A., Wendisch, M. and Rinke, A.:  
546 Surface impacts and associated mechanisms of a moisture intrusion into the Arctic observed in mid-April 2020 during  
547 MOSAiC. *Front. Earth Sci.*, 11, 1147848, <https://doi.org/10.3389/feart.2023.1147848>, 2023.  
548  
549 Kornhuber, K., Coumou, D., Vogel, E., Lesk, C., Donges, J.F., Lehmann, J., and Horton, R.M.: Amplified Rossby waves  
550 enhance risk of concurrent heatwaves in major breadbasket regions. *Nature Clim. Change*, 10, 48-53,  
551 <https://doi.org/10.1038/s41558-019-0637-z>, 2020.  
552  
553 Lee, S.H., and Butler, A.H.: The 2018-2019 Arctic stratospheric polar vortex. *Weather*, 75, 52-57,  
554 <https://doi.org/10.1002/wea.3643>, 2019.  
555  
556 Lee, S.H., Tippett, M.K., and Polvani, L.M.: A new year-round weather regime classification for North America. *J. Clim.*, 36,  
557 7091-7108, <https://doi.org/10.1175/JCLI-D-23-0214.1>, 2023.  
558  
559 Mattingly, K.S., Mote, T.L., and Fettweis, X.: Atmospheric river impacts on the Greenland Ice Sheet surface mass balance. *J.*  
560 *Geophys. Res. – Atmos.*, 123, 8538-8560, <https://doi.org/10.1029/2018JD028714>, 2018.  
561  
562 Meier, W.N., Fetterer, F., Windnagel, A.K., and Stewart, J.S.: NOAA/NSIDC Climate Data Record of Passive Microwave Sea  
563 Ice Concentration, Version 4. NSIDC: National Snow and Ice Data Center. <https://doi.org/10.7265/efmz-2t65>, 2021.  
564  
565 Meier, W.N., Stewart, J. S., Windnagel, A., and Fetterer, F. M.: Comparison of hemispheric and regional sea ice extent and  
566 area trends from NOAA and NASA passive microwave-derived climate records. *Remote Sens.*, 14, 619.  
567 <https://doi.org/10.3390/rs14030619>, 2022.  
568  
569 Meier, W.N., Petty, A., Hendricks, S., Kaleschke, L., Divine, D., Farrell, S., Gerland, S. Perovich, D., Ricker, R., Tian-Kunze,  
570 X., and Webster, M.: Sea Ice. NOAA Arctic Report Card 2023, R.L. Thoman, T.A. Moon, and M.L. Druckenmiller, Eds.,  
571 <https://doi.org/10.25923/f5t4-b865>, 2023.  
572  
573 Moore, G.W.K.: The December 2015 North Pole warming event and the increasing occurrence of such events. *Sci. Rep.*, 6,  
574 39084, <https://doi.org/10.1038/srep39084>, 2016.  
575  
576 Moore, G.W.K., Schweiger, A., Zhang, J., and Steele, M.: What caused the remarkable February 2018 north Greenland  
577 polynya? *Geophys. Res. Lett.*, 45, 1342-13350, <https://doi.org/10.1029/2018GL080902>, 2018.

578  
579 Nygård, T., Naakka, T., and Vihma, T.: Horizontal moisture transport dominates the regional moistening patterns in the Arctic.  
580 *J. Clim.*, 33, 6793-6807, <https://doi.org/10.1175/JCLI-D-19-0891.1>, 2020.  
581  
582 Overland, J.E., Ballinger, T.J., Cohen, J., Francis, J.A., Hanna, E., Jaiser, R., Kim, B.-K., Kim, S.-J., Ukita, J., Vihma, T.,  
583 Wang, M., and Zhang, X.: How do intermittency and simultaneous processes obfuscate the Arctic influence on midlatitude  
584 winter extreme weather events? *Environ. Res. Lett.*, 16, 043002, <https://doi.org/10.1088/1748-9326/abdb5d>, 2021.  
585  
586 Overland, J.E.: Arctic climate extremes. *Atmos.*, 13, 1670, <https://doi.org/10.3390/atmos13101670>, 2022.  
587  
588 Papritz, L., Hauswirth, D., and Hartmuth, K.: Moisture origin, transport pathways, and driving processes of intense wintertime  
589 moisture transport into the Arctic. *Weather Clim. Dyn.*, 3, 1-20, <https://doi.org/10.5194/wcd-3-1-2022>, 2022.  
590  
591 Serreze, M.C., and Barry, R.G. Processes and impacts of Arctic amplification: A research synthesis. *Glob. Planet. Change*, 77,  
592 85-96, <https://doi.org/10.1016/j.gloplacha.2011.03.004>, 2011.  
593  
594 Smith, K.L., Polvani, L.M., and Tremblay, L.B.: The impact of stratospheric circulation extremes on minimum Arctic sea ice  
595 extent. *J. Climate*, 31, 7169-7183, <https://doi.org/10.1175/JCLI-D-17-0495.1>, 2018.  
596  
597 Stroeve, J., and Notz, D.: Changing state of Arctic sea ice across all seasons. *Environ. Res. Lett.*, 13, 103001,  
598 <https://doi.org/10.1088/1748-9326/aade56>, 2018.  
599  
600 Tachibana, Y., Komatsu, K.K., Alexeev, V.A., and Ando, Y.: Warm hole in Pacific Arctic sea ice cover forced mid-latitude  
601 Northern Hemisphere cooling during winter 2017-18. *Sci. Rep.*, 9, 5567, <https://doi.org/10.1038/s41598-019-41682-4>, 2019.  
602  
603 Walsh, J.E., Ballinger, T.J., Euskirchen, E.S., Hanna, E., Mård, J., Overland, J.E., Tangen, H., and Vihma, T.: Extreme weather  
604 and climate events in northern areas: A review. *Earth-Sci. Rev.*, 209, 103324, <https://doi.org/10.1016/j.earscirev.2020.103324>,  
605 2020.  
606  
607 Wille, J.D., Favier, V., Dufour, A., Gorodetskaya, I.V., Turner, J., Agosta, C., and Codron, F.: West Antarctic surface melt  
608 triggered by atmospheric rivers. *Nature Geosci.*, 12, 911-916, <https://doi.org/10.1038/s41561-019-0460-1>, 2019.  
609  
610 Zhang, P., Wu, Y., Simpson, I.R., Smith, K.L., Zhang, X., De, B., and Callaghan, P.: A stratospheric pathway linking a colder  
611 Siberia to Barents-Kara sea ice loss. *Sci. Adv.*, 4, eaat6025, <https://doi.org/10.1126/sciadv.aat6025>.

612  
613 Zhang, P., Chen, G., Ting, M., Leung, L.R., Guan, B., and Li, L.: More frequent atmospheric rivers slow the seasonal recovery  
614 of Arctic sea ice. *Nature Clim. Change*, 13, 266-273, <https://doi.org/10.1038/s41558-023-01599-3>, 2023.  
615  
616 Zhou, S., Yu, B., and Zhang, Y.: Global concurrent climate extremes exacerbated by anthropogenic climate change. *Sci. Adv.*,  
617 9, eabo1638, <https://doi.org/10.1126/sciadv.abo1638>, 2023.  
618  
619 Zscheischler, J., Westra, S., van den Hurk, B.J.J.M., Seneviratne, S.I., Ward, P.J., Pitman, A., AghaKouchak, A., Bresch, D.N.,  
620 Leonard, M., Wahl, T., and Zhang, X.: Future climate risk from compound events. *Nature Clim. Change*, 8, 469-477,  
621 <https://doi.org/10.1038/s41558-018-0156-3>, 2018.  
622